

# Subduction earthquakes controlled by incoming plate geometry: The 2020 M>7.5 Shumagin, Alaska, earthquake doublet

Yu Jiang<sup>a</sup>, Pablo J. González<sup>a,b</sup>, Roland Bürgmann<sup>c</sup>

<sup>a</sup>COMET, Department of Earth, Ocean and Ecological Sciences, School of Environmental Sciences, University of Liverpool, Liverpool, L69 3BX, United Kingdom, [Yu.Jiang@liverpool.ac.uk](mailto:Yu.Jiang@liverpool.ac.uk)

<sup>b</sup>Volcanology Research Group, Department of Life and Earth Sciences, Instituto de Productos Naturales y Agrobiología (IPNA-CSIC), 38206 La Laguna, Tenerife, Canary Islands, Spain, [pabloj.gonzalez@csic.es](mailto:pabloj.gonzalez@csic.es)

<sup>c</sup>Department of Earth and Planetary Science, University of California, Berkeley, CA, USA, [burgmann@seismo.berkeley.edu](mailto:burgmann@seismo.berkeley.edu)

---

This manuscript is a preprint and has been submitted for publication in *Earth and Planetary Science Letters*. Please note that the manuscript is undergoing peer review and has not been accepted for publication. Subsequent versions of this manuscript may have slightly different content. If accepted, the final version of this manuscript will be available via the Peer-reviewed Publication DOI link on the right-hand side of this webpage. Please feel free to contact the corresponding author; we welcome feedback.

---

# Subduction earthquakes controlled by incoming plate geometry: The 2020 $M > 7.5$ Shumagin, Alaska, earthquake doublet

Yu Jiang<sup>a</sup>, Pablo J. González<sup>a,b</sup>, Roland Bürgmann<sup>c</sup>

<sup>a</sup>*COMET, Department of Earth, Ocean and Ecological Sciences, School of Environmental Sciences, University of Liverpool, Liverpool, L69 3BX, United Kingdom*

<sup>b</sup>*Department of Life and Earth Sciences, Instituto de Productos Naturales y Agrobiología (IPNA-CSIC), 38206 La Laguna, Tenerife, Canary Islands, Spain*

<sup>c</sup>*Department of Earth and Planetary Science, University of California, Berkeley, CA, USA*

---

## Abstract

In 2020, an earthquake doublet, a M7.8 on July 22nd and a M7.6 on October 19th, struck the Alaska-Aleutian subduction zone beneath the Shumagin Islands. This is the first documented earthquake doublet, of considerable size, involving a megathrust event and a strike-slip event, with both events producing deeply buried ruptures. The first event partially ruptured a seismic gap, which has not hosted large earthquakes since 1917, and the second event was unusual as it broke a trench-perpendicular fault within the incoming oceanic slab. We used an improved Bayesian geodetic inversion method to estimate the fault slip distributions of the major earthquakes using Interferometric Synthetic Aperture Radar (InSAR) wrapped phase and Global Navigation Satellite Systems (GNSS) offsets data. The geodetic inversions reveal that the Shumagin seismic gap is multi-segmented, and the M7.8 earthquake ruptured the eastern segment from 14 km down to 44 km depth. The coseismic slip occurred along a more steeply, 26-degree dipping

segment, and was bounded up-dip by a bend of the megathrust interface to a shallower 8-degree dip angle connecting to the trench. The model for the M7.6 event tightly constrained the rupture depth extent to 23-37 km, within the depth range of the M7.8 coseismic rupture area. We find that the M7.6 event ruptured the incoming slab across its full seismogenic thickness, potentially reactivating subducted Kula-Resurrection seafloor-spreading ridge structures. Coulomb stress transfer models suggest that coseismic and/or postseismic slip of the M7.8 event could have triggered the M7.6 event. This unusual intraslab event could have been caused by accumulation and localization of flexural elastic shear stresses at the slab bending region. We conclude that the segmented megathrust structure and the location of intraslab fault structures limited the rupture dimensions of the M7.8 event and are responsible for the segmentation of the Shumagin seismic gap. Our study suggests that the western and shallower up-dip segments of the seismic gap did not fail and remain potential seismic and tsunami hazard sources. The unusual earthquake doublet provides a unique opportunity to improve our understanding of the role of the subducting lithosphere structure in the segmentation of subduction zones.

*Keywords:* Subduction earthquake doublet, slab geometry, Shumagin seismic gap, Alaska subduction zone

---

## 1. Introduction

In 2020, a pair of large and similar sized earthquakes (doublet) occurred along the eastern Aleutian subduction zone off the Alaska Peninsula (Fig. 1(a)). The first and largest earthquake of the doublet, with a magnitude (M)

5 of 7.8, occurred at 06:12:44 UTC (22:12:44 local) on July 22 2020. On Oct  
6 19 2020 at 20:54:39 UTC (12:54:39 local), an anomalously large aftershock  
7 ( $M=7.6$ ) occurred 80 km southwest of the first event. According to the U.S.  
8 Geological Survey (USGS) hypocentre catalog, both earthquakes are located  
9 on the landward side of the subduction trench. The aftershocks of the first  
10 event are distributed parallel to the trench, while those of the second event  
11 are aligned perpendicular to the trench. The focal mechanism solutions from  
12 the Global Centroid Moment Tensor (GCMT) catalog suggest the mechanism  
13 of the M7.8 event is of thrust-faulting type, while the M7.6 event was a strike-  
14 slip event. The centroid depths of both earthquakes were estimated as about  
15 30-35 km. This suggests that the M7.8 event ruptured the buried megathrust  
16 interface, but the M7.6 event was caused by an unusual strike-slip rupture  
17 along an approximately trench-normal fault.

18 The 2020 Shumagin earthquake sequence is interesting for several reasons.  
19 Firstly, the mainshock is located within the Shumagin seismic gap. This  
20 portion of the subduction thrust has been identified as a seismic gap since  
21 the 1970s (Sykes, 1971, Davies et al., 1981). The seismic gap stretches  $\sim 200$   
22 km along the Shumagin Islands and is bounded to the west by the 1946  
23  $M_w 8.6$  earthquake (López and Okal, 2006) and to the east by the 1938  $M_w 8.2$   
24 rupture (Freymueller et al., 2021). The last earthquakes that are inferred  
25 to have ruptured through part of or the whole Shumagin gap occurred in  
26 1993, 1917, 1788, and possibly 1847 (Estabrook et al., 1994). Over the last  
27 century, a few moderate ( $M 6.5$  to  $M 7.0$ ) events have occurred in the area at  
28 depths greater than 30 km. However, the fault sections ruptured by those  
29 earthquakes are relatively small compared to the 200 km-long seismic gap



30 (e.g., the estimated rupture area of the 1993  $M_s$ 6.9 earthquake is 40 km-long  
31 and 15 km-wide, Lu et al. (1994)). If the whole Shumagin gap were fully  
32 locked, the accumulated moment equates to  $6.6 \times 10^{19}$  Nm/year, assuming a  
33 plate convergence rate of 64 mm/year and a uniform rigidity of 50 GPa. This  
34 would require a 7.5 event every 4 years, or a M8 event every 20 years. The lack  
35 of historic M7.5+ earthquakes in the Shumagin region has been explained due  
36 to substantial aseismic fault creep at seismogenic depths revealed by model  
37 inversions of inter-seismic GNSS velocities (Fournier and Freymueller, 2007).  
38 Fournier and Freymueller (2007) suggested that instead of rupturing in large  
39 earthquakes, most of the seismic moment in the Shumagin gap is released  
40 through steady creep. Thus, a moderate M7 earthquake every  $\sim 40$  years, as  
41 observed in the last century, may be sufficient to accommodate the residual  
42 slip deficit. To the west of the Shumagin gap, a recent interseismic coupling  
43 model shows that the shallow portion along the Sanak segment, 240 km-long  
44 and 115 km-wide, might be partially locked, with 15%-25% coupling (Drooff  
45 and Freymueller, 2021). For the shallow portion along the Sanak segment,  
46 if the estimated 1946 earthquake rupture area, 180 km-long and 115 km-  
47 wide (López and Okal, 2006), was fully locked, and the remaining area is  
48 20% coupled, the seismic moment deficit would be accumulating at around  
49  $4.5 \times 10^{18}$  Nm/year. This calculation suggests that the seismic moment of the  
50 1946 earthquake,  $8.5 \times 10^{21}$  Nm (López and Okal, 2006), releases 1900 years  
51 of elastic strain accumulation along the Sanak segment. Large uncertainties  
52 are associated with estimating earthquake recurrence intervals, including the  
53 poorly constrained estimation of the 1946 earthquake slip and the assumption  
54 of the highest slip deficit near the trench in the interseismic coupling model

55 (Drooff and Freymueller, 2021). Nevertheless, such long recurrence intervals  
56 could be the reason for there only being one documented major earthquake  
57 in the Sanak segment since 1700 (Estabrook and Boyd, 1992).

58 Secondly, the M7.6 slab-breaking aftershock had an unusual strike-slip  
59 mechanism and was deeply buried. Large oceanic lithosphere strike-slip  
60 events have previously occurred in the oceanic plate off subduction zones,  
61 such as the 2018  $M_w$ 7.9 Gulf of Alaska earthquake (Lay et al., 2018) and  
62 the 2012  $M_w$ 8.6 Wharton basin earthquakes off-Sumatra (Wei et al., 2013).  
63 In addition, the subduction zone outer-rise region regularly hosts normal-  
64 faulting mechanisms events. Outer-rise normal-faulting events are attributed  
65 to plate bending stresses from slab pull, and can be modulated by the in-  
66 terplate seismic cycle (Ammon et al., 2008). However, the occurrence of a  
67 major intraplate earthquake in the oceanic lithosphere just landward of the  
68 trench is rare, with only few reported examples, such as the October 4, 1994  
69  $M_w$ 8.2 earthquake off Shikotan Island along the Kuril trench (Tanioka et al.,  
70 1995). Another notable example was a  $M_w$ 7 strike-slip intraslab event lo-  
71 cated beneath Kodiak Island, Alaska down-dip of the locked portion of the  
72 Alaska-Aleutian megathrust (Hansen and Ratchkovski, 2001).

73 Thirdly, to our knowledge, these earthquakes are the first documented  
74 sizable earthquake doublet to involve a megathrust earthquake rupture, fol-  
75 lowed by an intraplate strike-slip earthquake tearing the subducting incom-  
76 ing slab. Earthquake doublets are pairs of events with comparable size and  
77 likely occur due to earthquake triggering interactions. Subduction earth-  
78 quake doublets have been studied in the 2006-2007 Kuril and 2009 Samoa  
79 doublets (Lay, 2015). In the 2006-2007 Kuril earthquake doublet, a  $M_w$ 8.4

80 megathrust earthquake was followed by a  $M_w$ 8.1 earthquake rupturing an  
81 outer trench-slope normal fault, while in the 2009 Samoa earthquakes, a  
82 normal-faulting earthquake ( $M_w$ 8.1) in the outer-rise region triggered a simi-  
83 larly sized thrust-faulting earthquake ( $M_w$ 8.0) on the plate interface (Beavan  
84 et al., 2010). Therefore, detailed documentation of this doublet might con-  
85 tribute to the general understanding of the triggering mechanisms during  
86 doublets.

87 In this paper, we use geodetic observations to determine kinematic co-  
88 seismic fault slip models of the M7.8, M7.6 earthquakes and the postseismic  
89 afterslip between two events. We investigate the major controls for the 2020  
90 Shumagin earthquake doublets. We analyze the static fault slip distribution  
91 of both events using static GNSS offsets and InSAR surface displacement  
92 measurements. The earthquakes ruptured an area off the Alaska Penin-  
93 sula covered with scattered islands, and incoherence due to water channels  
94 makes it challenging to estimate phase ambiguities during the InSAR phase  
95 unwrapping process. Hence, we take advantage of an improved Bayesian  
96 inversion of wrapped interferometric phase change observations (Jiang and  
97 González, 2020) to estimate the fault geometry and slip distribution. Our  
98 coseismic geodetic inversion results reveal that the Alaska megathrust has a  
99 complex down-dip segmentation. We propose a slab bend structure, which  
100 represents a major factor controlling the occurrence and interaction during  
101 this doublet, and contributes to the understanding of the mechanics of the  
102 subducting oceanic lithosphere in the central Alaska subduction zone.

## 103 **2. Datasets**

### 104 *2.1. GNSS dataset*

105 We used three-component coseismic offsets and postseismic time series  
106 from GNSS stations computed by the Nevada Geodesy Laboratory (Blewitt  
107 et al., 2018). The estimated coseismic offsets of the M7.8 event were derived  
108 from 5-minute sample rate time series of 108 GNSS stations, using 48 hours  
109 of data before and after the mainshock. The coseismic displacements were  
110 estimated by subtracting the median position after the mainshock from the  
111 median position before. The coseismic displacements of the M7.6 event were  
112 derived by subtracting the 24-hour final solutions of 97 GNSS station on  
113 October 19 from those on October 20. For the postseismic displacements  
114 between the M7.8 and M7.6 events, the displacements can be observed in  
115 the GNSS time series of daily solutions. Taking station AC12 as an example,  
116 the M7.8 postseismic horizontal displacements in the first day, 2 days, 24  
117 days and 48 days are 0%, 4%, 19%, and 25% of the coseismic horizontal  
118 displacements of the M7.8 event. Therefore, we model the 89-day postseismic  
119 deformation signal between July 22 to October 19 in the following way: (1)  
120 three-component daily solution of 21 GNSS stations less than 500 km away  
121 from the epicenter are downloaded; (2) a parametric model is fit to the  
122 time series from July 22 to October 19 with an exponential transient decay  
123 function (Hearn, 2003), to obtain estimates for the displacement magnitude  
124 for each station and a relaxation time (see Fig. S8); (3) we compute a  
125 parametric model of postseismic GNSS displacements between July 22 and  
126 October 19, and subtract the displacements on July 22 from those on October  
127 19.

128 *2.2. InSAR dataset*

129 We imaged the ground surface displacement caused by the 2020 Shumagin  
130 earthquake doublet using InSAR. Satellite radar interferograms capture line-  
131 of-sight (LOS) motion away or towards the satellite. We used 12 European  
132 Space Agency Sentinel-1 satellite interferometric wide swath mode images  
133 to make six interferograms from three different satellite tracks from July 10  
134 to November 7, 2020. We used data from two parallel descending tracks  
135 to cover the epicentral area around the Shumagin and neighboring islands  
136 (track 73 and track 102). The ascending track 153 fully images the epicentral  
137 area. We processed the coseismic interferograms using the TopsApp module  
138 of the ISCE software. We removed the topographic phase contribution in the  
139 interferograms using SRTM 30-m resolution digital elevation model.

140 Our interferograms (Table 1) spanning the M7.8 event are dominated by  
141 the coseismic deformation signals (Fig. 1(c)-(f)). We generate a preseismic  
142 interferogram (Fig. S1) which is dominated by the turbulent atmosphere  
143 phase delays. The two descending-track coseismic interferograms span less  
144 than 2 days of early postseismic deformation. However, for the coseismic  
145 interferogram in ascending track 153, the first available secondary image was  
146 acquired 48 days after the earthquake. Hence it could be affected by post-  
147 seismic deformation. We use the same strategy as described in Section 2.1  
148 to model the 48-day postseismic deformation signal (Fig. S9), and then we  
149 forward-simulate and remove the line-of-sight phase change from the ascend-  
150 ing interferogram (track 152, Jul 22-Sep 08) during the first 48 days of the  
151 postseismic period. Although, the correction is relatively small, our approach  
152 reduces the leakage of postseismic deformation into our coseismic models.

153 For the interferograms covering the M7.6 event, the interferometric phase  
154 observations are also dominated by the coseismic deformation signals. The  
155 estimated postseismic relaxation time for the M7.8 event is approximately  
156 40 days, while the acquisition dates of the primary images of the interfero-  
157 grams for the M7.6 event are 84 and 86 days after the M7.8 event, that is  
158 5 and 3 days before the M7.6. Therefore, any M7.8 postseismic deforma-  
159 tion signal can be considered negligible. The interferograms spanning the  
160 M7.6 event might contain 7, 9 and 19 days of postseismic deformation of  
161 this event. However, we did not find clear transient displacement signals ei-  
162 ther in the postseismic interferograms or GNSS time series during the M7.6  
163 early-postseismic period, so we performed no corrections on the coseismic  
164 interferograms.

### 165 **3. Methodology**

#### 166 *3.1. Fault geometry: Non-linear surface displacement inversion*

167 To determine the fault geometry of the ruptures, we invert for an elastic  
168 uniform slip rectangular dislocation model. First, we solve for the fault  
169 parameters using only the coseismic horizontal and vertical GNSS offsets  
170 using the GBIS package (Bagnardi and Hooper, 2018). However, the sparse  
171 spatial distribution of the GNSS stations does not allow to tightly constrain  
172 the fault geometry (Fig. S2). Thus, we take advantage of independent high-  
173 spatial-resolution InSAR observations over the Shumagin Islands and the  
174 imaged far-field surface deformation over the Alaska Peninsula to refine the  
175 rupture fault geometry.

176 Standard modeling approaches of InSAR observations require unwrap-  
177 ping the wrapped phase from  $[-\pi, \pi]$  to the absolute unwrapped LOS dis-  
178 placements. However, phase unwrapping is an ill-posed problem requiring  
179 integration along a path connecting pixels. In the Shumagin islands case,  
180 the incoherence due to water channels between islands makes the phase  
181 unwrapping especially challenging. Any phase unwrapping of coseismic in-  
182 terferograms might contain unknown multiples of  $2\pi$  between islands (see  
183 Fig. S12) due to the dense gradient of fringes. Instead, our method skips  
184 the phase unwrapping step, and directly inverts for fault source parameters  
185 by applying the WGBIS method, a Bayesian algorithm that minimizes the  
186 weighted wrapped phase residuals (Jiang and González, 2020). Now, using  
187 the wrapped InSAR phase and GNSS offsets, we can constrain more tightly  
188 the fault geometry parameters (Fig. 2).

### 189 *3.2. Distributed slip models*

190 Next, we propose an extension to the WGBIS method to estimate dis-  
191 tributed fault slip directly from InSAR wrapped phase observations applying  
192 a novel physics-based fault slip regularization. Traditional kinematic fault  
193 slip inversion method used static observations to solve for the slip displace-  
194 ments but neglected to consider the driving forces or stresses that cause these  
195 motions. Recently, a laboratory-derived crack model was introduced to de-  
196 scribe the relationship between stress and slip on the fault (Ke et al., 2020).  
197 Instead of a uniform stress drop across the whole fault plane, this model  
198 allows a constant stress drop in the crack center while keeping the stress  
199 concentration at the rupture tip finite, and it retains a smooth transition in  
200 between. The preferred shape of the crack model, an ellipse, is supported by

201 mechanical considerations (Sendekyj, 1970). Ke et al. (2020) proposed an  
 202 analytical model of the slip profile from the centre of the crack to the rup-  
 203 ture tip, and we expand this one-dimensional model into a two-dimensional  
 204 model with an elliptical shape, by assuming one of the focal points of the  
 205 ellipse to be the crack centre and the elliptical perimeter to be the crack tip.  
 206 Therefore, the slip distribution  $s$  on the fault plane is controlled by a very  
 207 reduced set of parameters, our crack model contains only seven parameters  
 208  $\mathbf{m}$ ,  $s = \mathbf{f}(\mathbf{m})$ .

$$\mathbf{m} = \{x_0, y_0, a, e, \lambda, d_{max}, \theta\} \quad (1)$$

209 where  $x_0, y_0$  are the locations of the focal point, and  $e$  is the eccentricity of  
 210 ellipse,  $\lambda$  is the ratio controlling the displacement transition from the center  
 211 to the edge of the elliptical crack,  $d_{max}$  is the maximum slip, and  $\theta$  is the rake  
 212 angle. We design synthetic tests (see Fig. S13) to validate our approach, and  
 213 compare the performance with respect other slip-inversion methods (Amey  
 214 et al., 2018).

215 We name our method, the Geodetic fault-slip Inversion using a physics-  
 216 based Crack MOdel, hereafter referred to as GICMo. The forward model  
 217 proceeds as follows: (1) the crack model parameters are provided and slips  
 218 for all fault patches are determined based on the two-dimensional crack model  
 219 discussed above; (2) the surface displacements are computed by integration  
 220 over the fault slip distribution set; (3) for the inversion, we follow Jiang  
 221 and González (2020), using a misfit function based on the wrapped phase  
 222 residuals and the weighting matrix of observations. This misfit function is  
 223 then regarded as the likelihood function, and used to retrieve the posterior  
 224 distribution of crack model parameters by a Bayesian sampling process.



225 We rationalize our choice for a simple elliptical crack model, firstly be-  
226 cause the resolution power of InSAR and GNSS data to constrain the sub-  
227 surface slip distribution decrease with the fault depth and off-shore distance.  
228 Deeper earthquake sources will produce less surface deformation than shal-  
229 lower events of the same size, and hence the detailed distributions of fault  
230 slip of deep sources are not well resolved. Second, the published M7.8 earth-  
231 quake coseismic slip distributions agree on the most notable feature: a high  
232 fault slip area with rather smooth slip distribution on the plate interface  
233 beneath the Shumagin Islands (Crowell and Melgar, 2020, Ye et al., 2021).  
234 This first-order pattern is well resolved by our GICMo model. Third, a sim-  
235 ple circular crack is also a widely accepted model to estimate the stress drop  
236 of earthquakes using the observed seismic spectra (Madariaga, 1976). In  
237 addition to the desirable physics-based properties (finite shear stress at the  
238 crack tip), another advantage of this method is its low dimensionality. The  
239 model is parametrized using fewer parameters than usually needed to de-  
240 scribe the spatial pattern of slip distributions. Previous inversion algorithms  
241 using deterministic or Bayesian approaches allow for highly complex patterns  
242 of slip distributions by allowing unconstrained or regularized slip distribu-  
243 tions (Fukahata and Wright, 2008). However, those methods are solving very  
244 high dimensional problems with larger associated null-spaces, and are also  
245 computationally more intensive.

### 246 *3.3. Coulomb stress models*

247 The Coulomb stress theory has been extensively applied to study the in-  
248 teraction between earthquakes. Coulomb stress change induced by fault slip  
249 is a quantitative measure that has been correlated with the aftershock dis-

250 tribution, seismicity rate changes and earthquake triggering. Usually, more  
251 aftershocks occur in the high stress-change region. It is thought that in-  
252 creases in Coulomb stress of 0.01 MPa are sufficient to trigger events (King  
253 et al., 1994). In our study, we calculate the Coulomb stress changes due to  
254 the M7.8 event and investigate whether the M7.8 earthquake and its afterslip  
255 promoted failure of the subsequent M7.6 event. We use the Coulomb 3.3 pro-  
256 gram to carry out the stress calculations, which is based on the dislocation  
257 model algorithms (<https://www.usgs.gov/software/coulomb-3>).

## 258 **4. Results**

### 259 *4.1. Coseismic model for the M7.8 earthquake*

260 The Shumagin earthquake nucleated near the eastern edge of the Shu-  
261 magin seismic gap (Davies et al., 1981). Our static surface displacement  
262 inversions suggest that the coseismic rupture extended for  $112\pm 2$  km to the  
263 WSW from the location of the USGS hypocentre (red rectangles in Fig. 2),  
264 with an average pure thrust slip of  $1.5\pm 0.1$  m, corresponding to an estimated  
265 M7.8. The buried rupture extended down-dip to  $44\pm 2$  km and up-dip up to  
266  $14\pm 2$  km depth and did not break the seafloor at the Alaska-Aleutian trench.  
267 This is consistent with reports of a minor tsunami (Ye et al., 2021). A re-  
268 markable feature of our inversion results is that the inferred fault geometry  
269 requires a relatively steep dip angle ( $26\pm 0.5$  degrees, Fig. 2(b)), steeper than  
270 the widely used Slab2 subduction model ( $\sim 15$  degrees, Hayes et al. (2018)).  
271 We further investigate this feature by separately inverting for the fault geom-  
272 etry using GNSS coseismic offsets only, InSAR wrapped phase only and both  
273 observations. In all cases, the obtained fault geometries are consistent with

274 a 25-to-28 degree fault rupture plane. The GNSS only inversion suggests a  
275 slightly steeper fault dip angle (Fig. S2), than the  $26\pm 0.5$ -degrees dip angle,  
276 obtained using only the InSAR wrapped phase or both datasets (Fig. S3-S4).

277 Next, we use our estimated fault geometry model to refine the location  
278 and pattern of coseismic slip during the earthquake. We tested two different  
279 3D fault geometry parameterizations. The first 3D fault geometry, based  
280 on the estimated fault geometry, contains two segments. A deeper segment  
281 dipping 26-degree from 14 km to 44 km depth using the optimal rectangular  
282 dislocation plane estimated by the non-linear inversion, and then a shallower  
283 segment connecting the top edge of the rectangular plane to the trench.  
284 These fault planes were then discretized into a triangular mesh with patch  
285 dimensions of  $\sim 5$  km. A second geometry was obtained based on the Slab2  
286 model for the Alaska megathrust, which has an average dip of 15 degrees  
287 from 20 km to 50 km (Hayes et al., 2018).

288 We solve for the slip distribution of our elliptical rupture model on the  
289 Slab2 and our proposed fault geometry (Fig. 2). Fig. 3 shows the observed  
290 and modeled GNSS displacements and the wrapped interferometric phase,  
291 as well as the residuals using the proposed down-dip structure. The modeled  
292 phase is consistent with the observed phase. The root-mean-square (RMS)  
293 of the GNSS residuals in the east, north and vertical directions are 0.3, 0.3  
294 and 0.6 cm, and corresponding to data variance reductions of 98%, 99%,  
295 and 97%. The GNSS offsets can be fit comparably well with both interface  
296 geometries (see Fig. S5-S7). However, the distributed slip model on the  
297 Slab2 geometry cannot reproduce the InSAR surface displacement patterns  
298 as well as those with the optimized, steeper fault geometry (Fig. 3, S5-S6).

299 Moreover, the posterior probability distribution functions on the elliptical  
300 rupture model parameters are less well resolved for the Slab2 fault parame-  
301 terization (Fig. S7). Our final slip model (Fig. 4(a)) shows a patch of large  
302 slip near the hypocenter and below the Shumagin Islands, consistent with  
303 kinematic coseismic slip models constrained using near-field high-rate GNSS  
304 and strong-motion data showing a more broadly distributed slip (Crowell and  
305 Melgar, 2020), and the finite-fault slip model using joint inversion of teleseis-  
306 mic P and SH waves and static displacements from regional GPS stations (Ye  
307 et al., 2021). The peak slip is 1.7 m, and the average slip is 0.7 m. The fault  
308 slip distribution inverted from GNSS and three interferograms is shown in  
309 Fig. 4(a). The total geodetic moment is  $6.12 \times 10^{20}$  Nm, which is equivalent  
310 to  $M_w$  7.79, a value consistent with the seismic moment magnitude of  $M_w$  7.8.  
311 The estimated rupture centroid is located at  $[158.834^\circ\text{W}, 55.130^\circ\text{N}]$  and the  
312 centroid focal depth is 32 km, which is deeper than the 28 km estimated by  
313 USGS and 19 km away from the USGS-estimated hypocenter,  $[158.596^\circ\text{W},$   
314  $55.072^\circ\text{N}]$ , in the northwest direction. Furthermore, as shown in Fig. 4(b),  
315 few aftershocks are located close to the slip peak, and most seismic events  
316 occurred near the edges of the estimated rupture area.

#### 317 *4.2. Postseismic model for the M7.8 earthquake*

318 The M7.8 postseismic phase is important to study the whole doublet se-  
319 quence, so we quantify the amount and distribution of early postseismic slip  
320 caused by the M7.8 event. As afterslip is unlikely to be compact, and may  
321 fully surround the coseismic rupture, the spatial distribution of postseismic  
322 slip is resolved by using the slip inversion package, slipBERI (Amey et al.,  
323 2018). This method incorporates the fractal properties of fault slip to regu-

324 larize the slip distribution. We assume that afterslip dominates the observed  
325 surface deformation during the 89-day-long period between the M7.8 and  
326 the M7.6 events. Afterslip describes postseismic aseismic fault motions oc-  
327 ccurring near the mainshock rupture regions over several months to several  
328 years. Postseismic offsets are estimated by fitting the daily GNSS data from  
329 July 22 to October 19 with a simple exponential model and then inverted  
330 for the postseismic slip distribution. Compared with the coseismic model 3D  
331 fault discretization, the subduction zone interface is extended along strike  
332 and down-dip to investigate the distributed postseismic slip over a wider  
333 area of the plate interface. The model predictions agree well with GNSS ob-  
334 servations (Fig. S8), and the RMS of the GNSS residuals in the east, north  
335 and vertical directions are 0.6, 0.6 and 0.7 cm, respectively.

336 We find the postseismic afterslip region mainly covered the deep portion  
337 ( $>50$ km depth) of the plate interface (Fig. S10 and orange lines in Fig.  
338 4(a)). A small patch, 60km-long and 40km-wide, is inferred to have slipped  
339 aseismically in the very shallow portion (6-9 km depth). In the depth range  
340 of 14-44 km, where the M7.8 earthquake ruptured, no strong afterslip is  
341 revealed. The 3-month postseismic slip has a cumulative geodetic moment  
342 of  $10^{20}$  Nm, corresponding to  $M_w$  7.27, assuming a variable crustal shear  
343 modulus with depth from CRUST 1.0. We try different slip variance values  
344 and rupture dimensions in slipBERI and it does not change those spatial  
345 characteristics substantially.

346 Crowell and Melgar (2020) estimated the first 10 days of the postseismic  
347 afterslip, finding that the majority of afterslip is concentrated downdip of  
348 the mainshock between 40-60 km depth. Their model is generally consistent

349 with our finding of afterslip dominantly occurring at greater depth. They also  
350 argued that although afterslip might occur up-dip of the M7.8 earthquake,  
351 the current configuration of GNSS stations is insensitive to the afterslip at  
352 shallow depth. Recently, Zhao et al. (*pers. comm., 2021*) applied additional  
353 constraints to regularize the afterslip distribution, where they considered  
354 both stress-driven frictional models and kinematic inversions in which no  
355 slip is allowed within the coseismic peak slip zone. The models of Zhao et  
356 al. (*pers. comm., 2021*) suggest possible afterslip in the up-dip area of the  
357 M7.8 earthquake.

#### 358 *4.3. Coseismic model for the M7.6 earthquake*

359 To parameterize the geometry of the October 19 2020 M7.6 Shumagin  
360 earthquake, we consider the spatial distribution of its aftershocks. Most of  
361 these aftershocks occurred at the western edge of the coseismic slip area of  
362 the M7.8 event. Aftershocks aligned in a north-south direction, parallel to  
363 the plate convergence direction. We first approximate the dimensions of the  
364 rupture area using the aftershock locations in the first two days after the  
365 M7.6 event. The estimated rupture area dimensions from the aftershocks are  
366 100-150 km long and 50-60 km wide and dipping 38 degrees to the east. Those  
367 parameters are consistent with the focal mechanism from GCMT catalog (dip  
368 angle=49°, strike angle=350°) and the inverted parameters for a rectangular  
369 dislocation source (length=50 km, width=20 km, top depth=23 km, bottom  
370 depth=37 km, dip angle=44.5°, strike angle=358.5°, strike slip=3.2 m). Our  
371 slip model reproduces well the coseismic deformation observed by GNSS and  
372 InSAR (Fig. 3 and Fig. S11).

373 The coseismic slip model shows right-lateral strike-slip motion on a fault

374 plane perpendicular to the Alaska subduction zone, consistent with the distri-  
375 bution of the aftershocks. The aftershocks following the M7.6 event occurred  
376 at the periphery of the coseismic rupture (Fig. 1(a)), effectively extending  
377 the latter farther to the south and were dominated by strike-slip rupture  
378 mechanisms with east-dipping north-south-striking nodal planes. The total  
379 moment release from the coseismic slip was  $2.1 \times 10^{19}$  Nm, assuming a vari-  
380 able crustal shear modulus with depth based on the CRUST 1.0 model. The  
381 corresponding moment magnitude is  $M_w=7.5$ , in reasonable agreement with  
382 the seismically determined value. We also estimated the stress drop to be 6.6  
383 MPa, which is within the usual bounds of intraplate earthquakes (Allmann  
384 and Shearer, 2009).

385 Our model suggests that the rupture zone is located from 23 km to 37 km  
386 in depth, beneath the slab interface (Fig. 2(c)). This reveals that the M7.6  
387 strike-slip earthquake ruptured the subducting oceanic slab, rather than the  
388 forearc. This is also confirmed from the focal depth range of the aftershocks.  
389 70% of the M2.5+ aftershocks in the first 2 days after the mainshock occurred  
390 at 20-40 km depth. A significant non-double-couple component in the mo-  
391 ment tensor, the substantial tsunami and the residuals of the GNSS vertical  
392 component (Fig. 3(d)) indicate that another shallow rupture segment paral-  
393 lel to the trench might exist (Lay, 2021), but our geodetic inversion cannot  
394 resolve a second segment at shallow depth. Our inversions for two segments  
395 using the geodetic data are not stable, which might be limited by the minor  
396 deformation signals on the islands.

397 **5. Discussion**

398 *5.1. Influence of slab geometry on the rupture characteristics of the M7.8*  
399 *earthquake*

400 Our preferred coseismic rupture model constrains the deep structure of  
401 the Alaska megathrust along the Shumagin segment. It reveals a  $\sim 26$  degrees  
402 dipping interface from 14 to 44 km depth. The megathrust interface at  
403 shallower depths is a gentler dipping segment ( $\sim 8 \pm 4$  degrees) of 90 km width,  
404 connecting the up-dip edge of the rupture to the trench (Fig. 2). This plate-  
405 interface geometry substantially deviates from the most recent subduction  
406 interface model Slab2, which is based on regionally and globally located  
407 seismic events (Hayes et al., 2018). The Slab2 model suggests a 15-degrees  
408 dip in the depth range from 20 to 50 km. This might indicate that the steeper  
409 segment could be a relatively localized structural feature along this section  
410 of the subduction zone. The discrepancy with the Slab2 model might be  
411 due to smoothness constraints applied to the subduction zone model, which  
412 might not resolve length-scales similar or smaller than those of the Shumagin  
413 gap (100-200 km). This highlights the need to create additional regional  
414 models that capture finer spatial structural details to improve subduction  
415 zone seismic hazard assessment.

416 Seismic reflection imaging along profiles across the Shumagin segment  
417 suggests a geometry similar to our inversion results (Li et al., 2015). In  
418 Fig. 2(b), we show the interpreted seismic reflection data from Line 4 of  
419 Li et al. (2015). Line 4 is located in the proximity of the M7.8 rupture  
420 area, at the boundary of the Semidi segment and Shumagin seismic gap.  
421 The seismic reflectors are consistent with our inferred fault geometry. Our



422 plate interface geometry also agrees with a fault geometry grid search using  
423 GNSS vertical coseismic offsets caused by the M7.8 earthquake by Crowell  
424 and Melgar (2020). Their dislocation models also support a 25-degree dip  
425 fault geometry, with an up-dip edge at  $21\pm 2$  km and extending down to  $45\pm 5$   
426 km depth.

427 We also note that the M7.8 down-dip rupture limit approximately coin-  
428 cides with the depth of the continental Moho, imaged by the seismic reflection  
429 data at 39-41 km depth. This is consistent with a first-order correlation of  
430 the base of the seismogenic zone and the base of the continental crust (e.g.,  
431 Oleskevich et al. (1999)), but exceptions to this pattern have been noted  
432 (Simoes et al., 2004). A zone of low-frequency tremor sources (Brown et al.,  
433 2013) is located at  $\sim 50$  km depth, and there is a gap between the seismo-  
434 genic zone and the area hosting tremor, which is also observed in the Nankai  
435 and Cascadia subduction zones (Gao and Wang, 2017). The bottom of the  
436 rupture likely reached the down-dip limit of the locked seismogenic zone.  
437 Recently, Shillington et al. (2021) analyzed the seismic reflection data from  
438 nearby Line 5 (Fig. 2(a)) and found the continental Moho depth at 35 km,  
439 with less uncertainties than Line 4 (Li et al., 2015). If this is confirmed,  
440 it might suggest that part of the coseismic slip extended downdip of the  
441 continental Moho (or mantle wedge corner). This coseismic slip feature was  
442 previously observed in very large megathrust events, e.g. the 2010 M8.8  
443 Maule, Chile, earthquake (Weiss et al., 2019). One of the explanations could  
444 be that hydrated materials (e.g., serpentinites) along the base of the man-  
445 tle wedge control the frictional properties of the megathrust, and allow the  
446 propagation of large ruptures, even though the megathrust downdip of the

447 mantle wedge corner is predominantly velocity strengthening (Wang et al.,  
448 2020, Kohli et al., 2011).

449 Our findings suggest that the fault geometry controls the rupture size  
450 and extent. A similarly large buried rupture was observed during the 2015  
451 Gorkha, Nepal earthquake on a continent-continent subduction zone (Elliott  
452 et al., 2016). Hubbard et al. (2016) developed a fault morphological model  
453 consisting of two ramps and found that the location and shape of coseis-  
454 mic fault slip ( $>1\text{m}$ ) match well with the location and shape of the middle  
455 decollement bounded on both sides by ramps. Therefore, they proposed that  
456 the variations in fault dip angle controlled the shape and size of the main-  
457 shock rupture in this continental megathrust earthquake. Decollement-ramp  
458 structures formed in subducting sediments are not rare in global subducting  
459 zones (Seno, 2017). About 1-km-thick subducting sediments were inferred  
460 from seismic reflection data beneath the eastern Shumagin gap (Li et al.,  
461 2018) and clear variations of the megathrust dipping angle were revealed at  
462 7 km and 17 km (Li et al., 2015), which is consistent with the top rupture  
463 depth at 14 km. In summary, the variation in fault orientation with depth  
464 was likely a controlling factor limiting the extent of the Shumagin rupture.

### 465 *5.2. The M7.6 slab-tear earthquake source region*

466 If we assume that the M7.6 earthquake occurred on a pre-existing fault  
467 plane, this fault had a 16-degree strike and 60-degree dip prior to being  
468 subducted. This strike angle is consistent with the strike of the Kula-  
469 Resurrection ridge (Fig. 6(a), Fuston and Wu (2020)). These ridges were  
470 active from 60 to 40 Ma, producing north-south striking faults through the  
471 seafloor spreading, and have been inactive since  $\sim 40$  Ma. The inferred dip-

472 ping angle of the pre-existing fault is consistent with the dip angle of mid-  
473 ocean-ridge normal faults. The pre-existing faults are unlikely to be formed  
474 in the outer-rise region because the outer-rise bending faults are parallel to  
475 the trench with approximately east-west strike directions (Shillington et al.,  
476 2015). The pre-existing faults are unlikely to have formed along the Pacific-  
477 Kula ridge or the Pacific-Farallon ridge, because the orientation of the mag-  
478 netic anomalies (east-west and northwest-southeast) are inconsistent with  
479 the eventual strike of the M7.6 ruptured fault.

480 In addition, our M7.6 fault model is correlated with the location of a  
481 low seismic-velocity anomaly, which has been attributed to higher slab hy-  
482 dration (Li et al., 2020). Li et al. (2020) imaged the crust and uppermost  
483 mantle structure of the Alaska subduction zone using ocean bottom seismo-  
484 graphs and broadband seismic stations. They constructed a 3-D shear veloc-  
485 ity model, where one trench-normal profile (TT1) is just  $<5$  km away from  
486 the M7.6 rupture area. They found upper mantle shear-velocity reductions  
487 along this profile of about 15% (from  $\sim 4.6$  to  $\sim 3.9$  km/s), which extends  
488 more than 12 km beneath the Moho. In other regions along the Alaska sub-  
489 duction zone (e.g., Semidi segment), the upper mantle velocity reduction is  
490 only about 11% (from  $\sim 4.6$  to  $\sim 3.9$  km/s). They interpret this feature as  
491 evidence of stronger hydration of the incoming plate along the Shumagin  
492 seismic gap. Furthermore, in the outer-rise region of the Shumagin Islands  
493 (Line 5 in Fig. 2(a) and Fig. 4(a)), Shillington et al. (2015) found a P-wave  
494 velocity reduction in the upper mantle from 8.25 to 7.75 km/s, associated  
495 with abundant bending faults. These observations lend further support to  
496 the existence of faults in the subducted slab beneath the Shumagin Islands,

497 which might have played a major role in the location of seismogenic ruptures.

498 Here, we propose a simple mechanical model that partially explain the  
 499 location of the M7.6 event. As previously shown, the M7.6 strike-slip event  
 500 ruptured the incoming slab near a bend in the down-dip geometry of the  
 501 plate interface. This bend could localize deformation. Knowing that sub-  
 502 ducting lithosphere is subject to flexural bending shear stresses, which are  
 503 large enough to break the crust in the outer-rise region, we propose that  
 504 the M7.6 could have partially been caused by accumulated flexural bending  
 505 shear stresses in addition to lateral stress loading variations along the trench.  
 506 Here, we assume that the rheological behaviour of the oceanic lithosphere can  
 507 be approximated by that of an elastic beam. The deflection of the oceanic  
 508 lithosphere is, to the first order, controlled by the gravitational body forces  
 509 and bending moment acting on the descending plate (Fig. 5). So, we can  
 510 compute the shear stress rate  $dV$  acting on the elastic lithosphere as a func-  
 511 tion of the distance from the trench,  $X$  (Turcotte and Schubert, 2014):

512

$$dV = \frac{\sqrt{2}\pi^3 e^{\pi/4}}{32A} \frac{Dw_b}{(X_b - X_0)^3} \left[ \cos \left\{ \frac{\pi(X - X_0)}{4(X_b - X_0)} \right\} + \sin \left\{ \frac{\pi(X - X_0)}{4(X_b - X_0)} \right\} \right] \exp \left[ -\frac{\pi(X - X_0)}{4(X_b - X_0)} \right] \quad (2)$$

513 where  $X_0$  is the location of the trench,  $X_b$  is the location deflection forebulge  
 514 with height  $w_b$ , and  $A$  is the slab age. The flexural rigidity parameter,  $D$   
 515 is given by the expression  $D = \frac{ET_e^3}{12(1-\nu^2)}$ , which is a function of the effective  
 516 elastic thickness ( $T_e$ ), the Young's modulus ( $E$ ) and the Poisson's ratio ( $\nu$ ).  
 517 To simulate the shear stress rate  $dV$  acting on the Shumagin segment, we  
 518 use parameters from Zhang et al. (2018) as listed in Table 2. The estimated  
 519 shear stress rate at the location and along the length of the M7.6 rupture  
 520 fault varies from 0.006 to 0.05 MPa/year. If we compare these values with

521 respect to the coseismic stress drop, 6.6 MPa, the M7.6 event could have  
522 released 130~1100 years of accumulated bending shear stress. In addition  
523 to flexural bending shear stress, shear stress directions could be controlled  
524 by the slab geometry variations along trench-parallel direction. For example,  
525 the downdip plate geometry from 10-50km depth along Line 5 (Shillington  
526 et al., 2021) is smoother than that along Line 4 (Li et al., 2015).

527 Alternatively, shear stresses could be caused by spatial variations of elas-  
528 tic coupling along the megathrust interface. Herman and Furlong (2021)  
529 present models that simulate the effect of laterally variable coupling. The  
530 preferred models represent the Semidi segment to be highly coupled while  
531 the Shumagin segment has low coupling. The lateral displacement variations  
532 can impose large-magnitude, right-lateral shear stresses on the M7.6 rupture  
533 plane geometry, assuming the target fault plane was north-south striking  
534 and east dipping with a dip angle  $50^\circ$ . However, we note that the available  
535 geodetic observations infer only  $30\% \pm 10\%$  coupling in the western portion  
536 of Semidi segment (Drooff and Freymueller, 2021) which is much lower than  
537 the 100% assumed by Herman and Furlong (2021), for the whole Semidi  
538 segment. Therefore, interseismic coupling variation between the Semidi and  
539 Shumagin segments may contribute to the shear stress accumulation on the  
540 M7.6 rupture plane, but geodetic evidence suggests this contribution may be  
541 more modest in magnitude. Hence, lateral variations of coupling, the exis-  
542 tence of structural weaknesses and long-accumulated bending flexural shear  
543 stress could explain the occurrence of the M7.6 slab breaking event, which  
544 broke the entire seismogenic thickness.

545 *5.3. Mechanisms for the interaction between the two earthquakes*

546 Earthquake doublets are not uncommon and suggest short-term fault in-  
547 teractions and triggering. Lay (2015) compiled 7 pairs of earthquake doublets  
548 in subduction zones, where he proposed that stress transfer and triggering  
549 interactions are clearly demonstrated by several doublet sequences and the  
550 complexity of faulting of many of the events. To investigate the possible  
551 relationship between these events, we calculate the stress perturbations on  
552 the M7.6 event associated with the Jul 22 2020 M7.8 coseismic and post-  
553 seismic slips (Fig. 4(d)). We utilize the inferred slip distribution from our  
554 inversion model for the M7.8 event. Then, we compute the stress change on  
555 the estimated fault plane of the M7.6 event. We extend the M7.6 rupture  
556 fault plane along dip from the surface down to 60 km depth, and compute  
557 the stress change on a regular grid with 5 km-wide patches. The M7.8 earth-  
558 quake caused a shear stress increase of 0.07 MPa and tensile normal stress  
559 increase of 0.27 MPa around the hypocenter, while the contributions from  
560 the postseismic slip are almost neutral. Our Coulomb stress models suggest  
561 that the second, M7.6 intraslab, earthquake was likely triggered by the elas-  
562 tic stress changes transferred by the slip during the M7.8 coseismic slip on  
563 the megathrust interface, with postseismic deformation processes possibly  
564 explaining the  $\sim 3$ -month delay in the occurrence of the large intraslab event.

565 **6. Conclusions**

566 We conclude that the 2020 Shumagin earthquake doublet represents a  
567 rare example of two deeply buried ruptures on a subduction megathrust and  
568 an oceanic intraplate strike-slip fault (Fig. 6(b)). The first M7.8 earth-

569 quake partially ruptured the Shumagin seismic gap, along a 112 km-long, 65  
570 km-wide section, extending from 14 km to 44 km depth. The second M7.6  
571 event was likely triggered by static stress changes due to the M7.8 coseismic  
572 slip and could have released 130~1100 years of accumulated flexural bend-  
573 ing shear stresses. The M7.6 broke the incoming oceanic plate at moderate  
574 depths from 23 km to 37 km along a north-south striking and east-dipping,  
575 right-lateral strike-slip fault. We propose that the Shumagin gap is seg-  
576 mented and has variable mechanical characteristics. The M7.8 earthquake  
577 ruptured a distinct eastern segment of the Shumagin gap, while the western  
578 segment and shallow portions remain unruptured. We highlight that the in-  
579 ferred rupture geometry of the M7.8 event is substantially steeper compared  
580 to the Slab2 model. The variations of down-dip megathrust structure of the  
581 Shumagin segment might have implications for seismo-tectonics and tsunami  
582 hazard of this segment of the Alaska-Aleutian subduction zone, e.g., by con-  
583 trolling the degree of coupling and seismic segmentation of the megathrust  
584 interface (Fournier and Freymueller, 2007, Hayes et al., 2018), and influenc-  
585 ing coseismic and postseismic slip distributions (Crowell and Melgar, 2020).  
586 In addition, we identify Kula-Resurrection ridge fault structures imprinted  
587 in the oceanic lithosphere as the likely earthquake source plane reactivated  
588 during the M7.6 event. Our study highlights that the reactivation of such  
589 oceanic lithospheric structures might pose an important seismic hazard in  
590 subduction zones, and might represent favorable pathways for fluid flow and  
591 dehydration of the subducting slab.

## 592 7. Acknowledgments

593 This research was supported by the Natural Environmental Research  
594 Council (NERC) through the Centre for the Observation and Modelling  
595 of Earthquakes, Volcanoes and Tectonics (GA/13/M/031) and the LiCS  
596 large grant (NE/K011006/1). This research was also supported by a Chi-  
597 nese Scholarship Council-University of Liverpool joint scholarship awarded  
598 to YJ (201706450071). PJG contribution was supported by the Spanish  
599 Ministerio de Ciencia e Innovación research project, grant agreement num-  
600 ber PID2019-104571RA-I00 (COMPACT) and the Beca Leonardo a Investi-  
601 gadores y Creadores Culturales 2020 of the Fundación BBVA. RB acknowl-  
602 edges support by NSF award EAR-1801720. Copernicus SAR data are re-  
603 trieved from [scihub.copernicus.eu](https://scihub.copernicus.eu), and 6 interferograms as well as the  
604 information of 12 SAR images can be downloaded from Zenodo (<https://doi.org/10.5281/zenodo.xxx>). The 108 and 97 GNSS stations with three-  
605 component coseismic offset estimates for Jul 22 2020 M7.8 event and Oct 19  
606 2020 M7.6 event are retrieved from [http://geodesy.unr.edu/news\\_items/20200723/us7000asvb\\_5min\\_rapid\\_20200723.txt](http://geodesy.unr.edu/news_items/20200723/us7000asvb_5min_rapid_20200723.txt) and <http://geodesy.unr.edu/>. The 21 GNSS stations with three-component daily offsets to estimate  
607 the postseismic decay time are retrieved from Nevada Geodetic Laboratory  
608 (<http://geodesy.unr.edu/>). The Subduction zone geometry model is re-  
609 trieved from Slab2 (<https://www.sciencebase.gov/catalog/item/5aa1b00ee4b0b1c392e86467>).  
610 The bathymetry data is retrieved from SRTM30\_PLUS ([https://topex.ucsd.edu/WWW\\_html/srtm30\\_plus.html](https://topex.ucsd.edu/WWW_html/srtm30_plus.html)). The earthquake catalog is re-  
611 trieved from USGS (<https://earthquake.usgs.gov/earthquakes/search/>).  
612 The coastal data is retrieved from NOAA (<https://www.ngdc.noaa.gov/>



617 [mgg/shorelines/](#)). This is a contribution of the CSIC Thematic Platform  
618 PTI-Teledect (<https://pti-teledetect.csic.es/>). CRUST 1.0 model is  
619 retrieved from <https://igppweb.ucsd.edu/~gabi/crust1.html>.

Table 1: Details of Sentinel-1 interferograms for 2020 Shumagin earthquake doublet, M7.8 and M7.6 event.

Earthquake date and magnitude	Track no.	Direction (asc/des)	Incidence (degree)	Primary image (yyyy/mm/dd hh:mm:ss)	Secondary image (yyyy/mm/dd hh:mm:ss)
2020/07/22 06:12:44 M7.8	73	des	30-33	2020/07/10 17:03:59	2020/07/22 17:04:00
	102	des	43-46	2020/07/12 16:47:32	2020/07/24 16:47:33
	153	asc	36-41	2020/07/22 04:23:36	2020/09/08 04:23:39
2020/10/19 20:54:38 M7.6	73	des	30-35	2020/10/14 17:04:04	2020/10/26 17:04:04
	102	des	43-46	2020/10/16 16:47:36	2020/10/28 16:47:36
	153	asc	34-41	2020/10/14 04:23:40	2020/11/07 04:23:40

Table 2: Variables for shear stress rate calculation (Zhang et al., 2018)

Symbol	Variables	Value	Unit
$E$	Young's modulus	$7 \times 10^{10}$	Pa
$\nu$	Poission's ratio	0.25	-
$T_e$	Effective thickness of oceanic lithosphere	18.2	km
$w_b$	Height of the forebulge	0.18	km
$x_0$	Location of the trench	0	km
$x_b$	Location where the deflection is $w_b$	42.7	km
$A$	Plate age	54	Ma

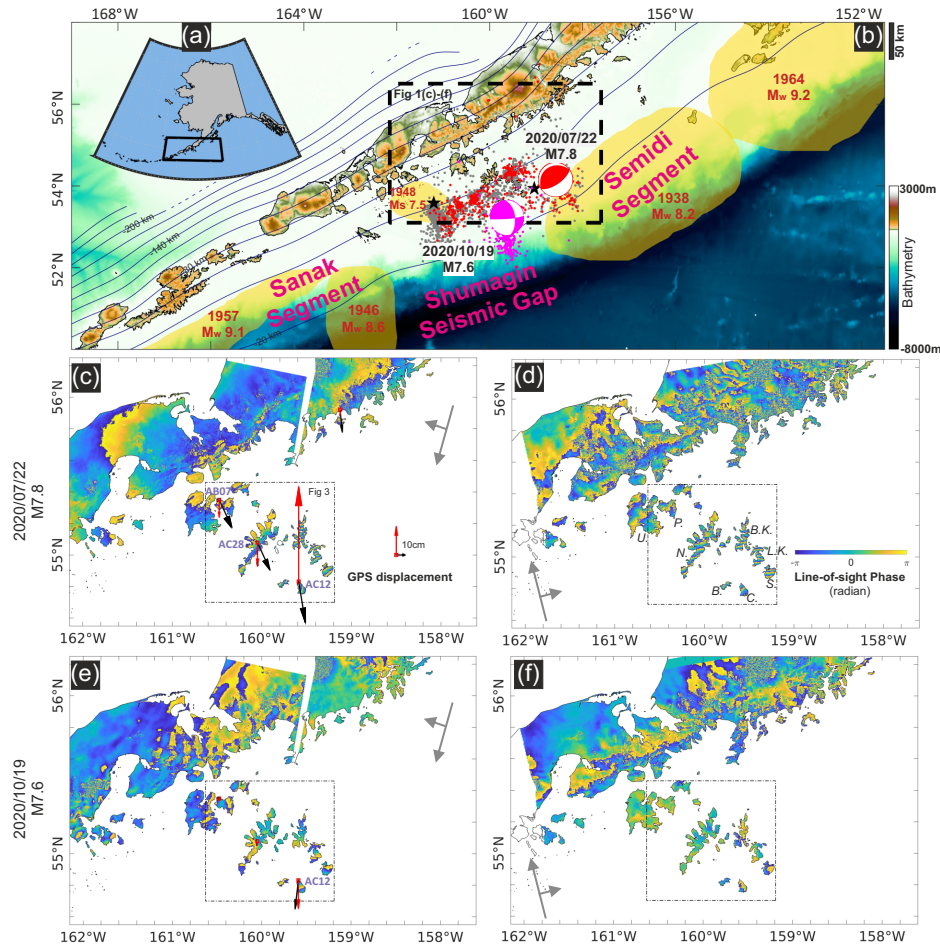


Figure 1: Tectonic background and geodetic observations of the Shumagin earthquake doublet, 2020/07/22 M7.8 earthquake and 2020/10/19 M7.6 earthquake. (a) inset shows the Aleutian subduction zone. Panel (b) shows historic ruptures as shaded yellow areas, on top of the bathymetry as the background. The Shumagin seismic gap is the 200 km-long region between the 1946  $M_w$ 8.6 and the 1938  $M_w$ 8.2 earthquakes. The M7.8 and the M7.6 events are plotted as red and magenta beachballs. The first 2-day and 3-month aftershocks following the M7.8 event are plotted as red and gray dots, where two M6+ events are plotted as little black stars. The first 2-day aftershocks following the M7.6 event are plotted as magenta dots. The dashed box shows the boundary for images (c)-(f). Panel (c) shows the wrapped phase of two descending interferograms, 2020/07/10-2020/07/22 (Track 73) and 2020/07/12-2020/07/24 (Track 102). The arrows show the GNSS

Figure 1 (continued): displacements retrieved from Nevada Geodesy Laboratory, red for vertical, and black for horizontal displacements. AB07, AC28 and AC12 are three GNSS stations with the most significant movement. GNSS displacement at [158.5W,55N] is the unit displacement vector for 10cm vertical and horizontal displacement. The dotted-dashed box marks area in Fig. 3. Panel (d) shows the ascending interferogram 2020/07/22-2020/09/08 from track 153. Panel (e) and (f) is same with Panel (c) and (d), but three interferograms covering the M7.6 event, of two descending interferograms, 2020/10/14-2020/10/26 (Track 73) and 2020/10/16-2020/10/28 (Track 102), and one ascending interferogram, 2020/10/14-2020/11/07 (Track 153). Island abbreviations: U.: Unga; P.: Popof; N.: Nagai; B.K.: Big Koniuji; L.K.: Little Koniuji; B.: Bird; C.: Chernabura; S.: Simeonof.

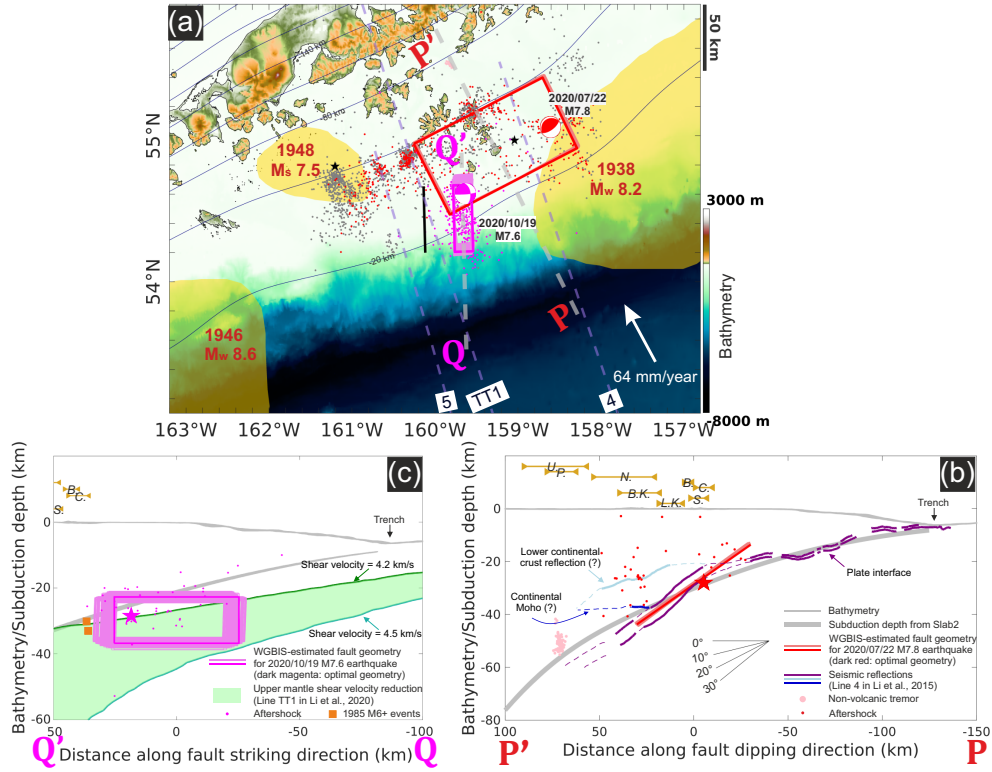


Figure 2: Preferred geodetic fault model constrained using InSAR wrapped phase and GNSS. In panel (a), red and magenta rectangles outline the ensemble of inverse bayesian fault geometry models for the M7.8 and the M7.6 earthquakes. The black line west of the magenta rectangle indicates its projection to the surface. The dashed purple lines 4, 5 and line TT1 indicate the position of a seismic reflection line from Li et al. (2015) and a shear velocity profile from Li et al. (2020); the dashed gray lines are profiles PP' and QQ' shown in (b) and (c). Panel (b) shows a cross-section of the inferred fault geometry models of the M7.8 earthquake projected to profile PP'. We also show the geophysical interpretation of the reflection lines (Line 4 and Fig. 5 in Li et al. (2015)), and locations of tremor (Brown et al., 2013). The cross-section also shows Slab2 model (depth to the top of subducting plate) and the bathymetry along profile PP'. Brown lines show the projected location of islands with the same abbreviations as Fig. 1(d). Panel (c) shows a cross-section of the inferred fault geometry models of the M7.6 earthquake projected to profile QQ'. We also show the shear velocity reduction zone within upper mantle, constrained by the shear

Figure 2 (continued): velocity 4.2 km/s and 4.5 km/s and digitized from Li et al. (2020). Two orange blocks present the M6+ subducting events in 1985 <5 km from the northern end of the fault model (<https://earthquake.usgs.gov/earthquakes/eventpage/usp0002kmh/executive>, <https://earthquake.usgs.gov/earthquakes/eventpage/usp0002msj/executive>).

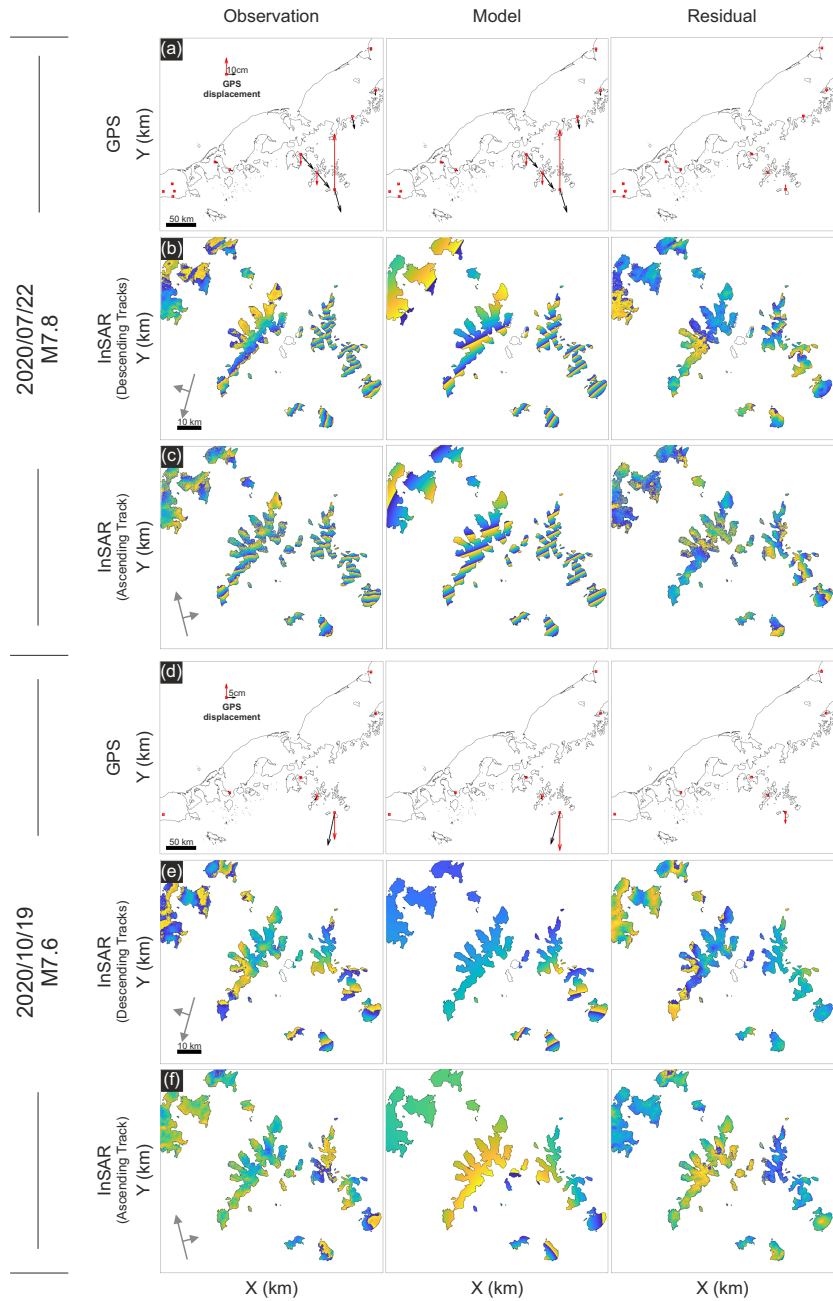


Figure 3: The observed and modelled GNSS displacements and wrapped interferometric phase. Images in the left column present the GNSS observations and the observed wrapped phase for the interferograms along 2 descending tracks, as shown in the dotted-dashed box in Fig. 1(c)-(f). Images in the middle column are the modelled GNSS and wrapped phase based on the optimal slip distributions. Images in the right column are the residual between observations and model.

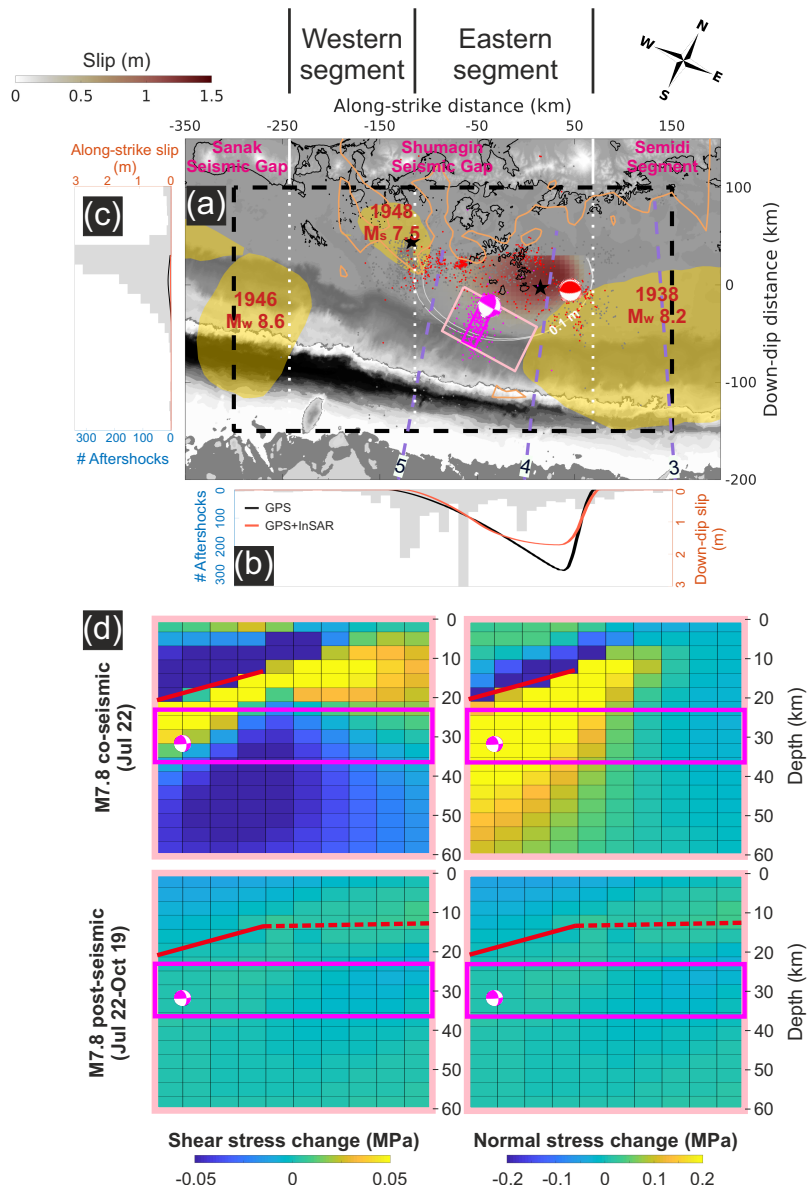


Figure 4: 2020 Shumagin earthquake doublet inferred fault slip and aftershock distribution. Panel (a) presents the coseismic slip distribution estimated from GNSS offsets and interferograms. The map is rotated so the along-strike slip is parallel to the x-axis and along-dip slip to the y-axis. White thin lines correspond to the 0.5m slip contours for minimum and maximum acceptable model parameters illustrating the uncertainties in the estimated coseismic rupture models of the Jul 22 2020 M7.8 event, and white thick lines



Figure 4 (continued): are the 0.25m slip contours for the postseismic slip models of this event (Jul 22- Oct 19 2020). Dashed white lines divide the Shumagin gap into two segments, discussed in the main text. Dashed purple lines mark seismic reflection lines 3-5 in Li et al. (2015) and Shillington et al. (2015), located in the Semidi Segment and eastern and western segments of Shumagin gap. The M7.8 and the M7.6 events are plotted as red and magenta beachballs. The first 2-day and 3-month aftershocks following the M7.8 event are plotted as red and gray dots, where two M6+ events are plotted as little black stars. The first 2-day aftershocks following the M7.6 event are plotted as magenta dots. Magenta rectangle outlines the ensemble of inverse Bayesian fault geometry model for the M7.6 earthquake, and the pink rectangle is the extended model from the surface (depth=0) to depth=60 km. Panels (b) and (c) show the slip and aftershock distributions in the along-strike and along-dip directions, with gray bars showing the number of aftershocks in 10 km-wide intervals. Black and orange lines show slip profiles from GNSS only and GNSS and InSAR data inversions, respectively. Image (d) presents the stress change on the extended geometry of the M7.6 fault model, caused by the M7.8 coseismic and postseismic slip distributions shown in (a). Solid red lines from 14-20 km present the intersection of two fault planes.

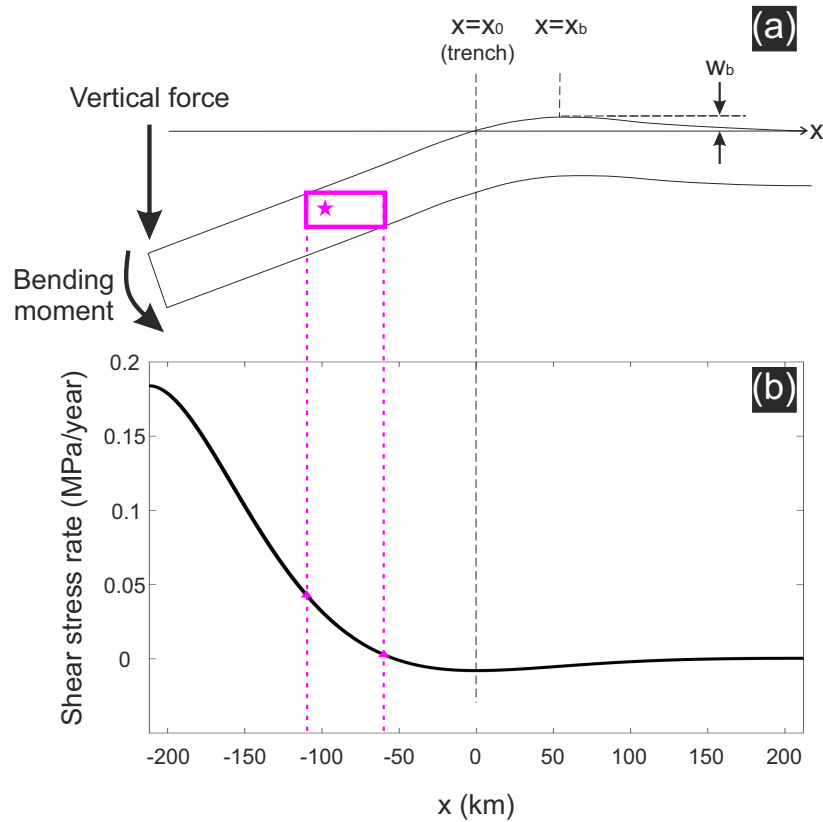


Figure 5: Bending of the lithosphere at an ocean trench due to an applied vertical load and bending moment. Image (a) is the conceptual model lithosphere bending, which is modified from Fig. 3.33 in Turcotte and Schubert (2014). Image (b) is the estimated shear stress rate along the trenching-normal profile.

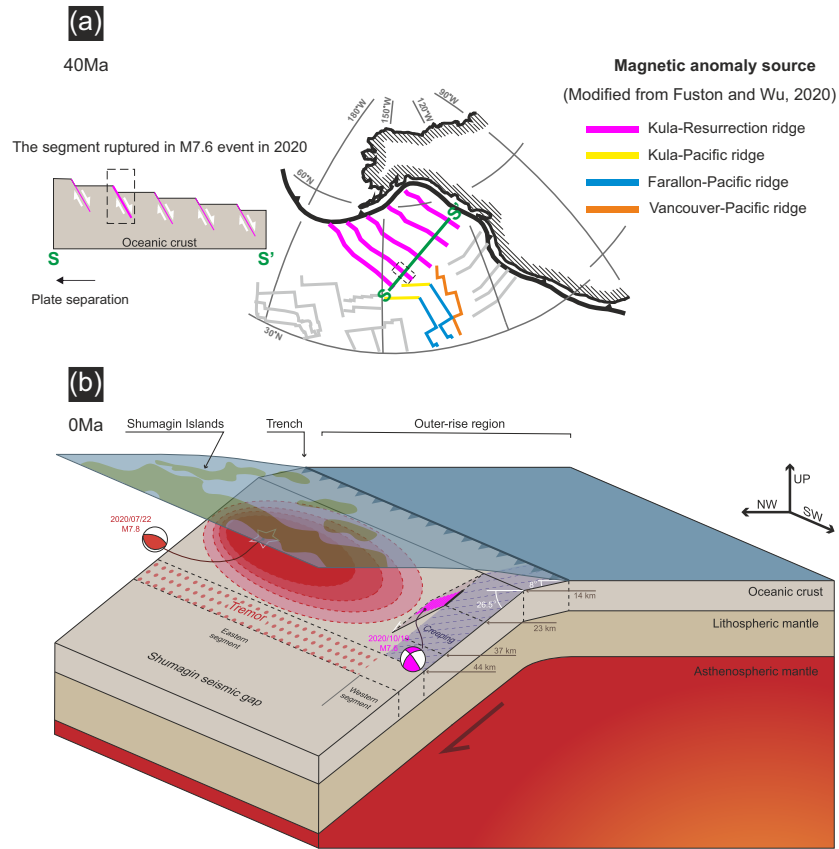


Figure 6: Conceptual model of the main subduction zone characteristics where the megathrust earthquake occurs in the plate interface and the triggered strike-slip earthquake tears the incoming oceanic lithosphere. Image (a) shows the slab plate tectonic reconstruction of western North America at 40Ma, modified from Fuston and Wu (2020). The magenta lines indicated the magnetic anomalies caused by the Kula-Resurrection ridge, which was subducted beneath the Aleutian Islands in the present days. A cross-section of this series of magnetic anomalies are plotted in profile SS'. We propose that a normal fault associated with this ridge system was reactivated in the Oct 19 2020 M7.6 earthquake. Yellow, blue and orange lines present the magnetic anomalies caused by Kula-Pacific ridge, Farallon-Pacific ridge, and Vancouver-Pacific ridge. This Pacific-Farallon-Kula triple junction moved to the north with the subducting Pacific plate and is located in the outer-rise region close to Shumagin Islands now. In image (b), the red shaded region is the rupture area at depth 14-44 km caused by the Jul 22 2020 M7.8 event. The magenta shaded region

Figure 6 (continued): is the rupture area caused by the Oct 19 2020 M7.6 event. The latter fault might be a reactivated pre-existing fault before subducting, caused by the seafloor spreading of Kula-Resurrection ridge, as shown in image (a).

620 **References**

621 L. R. Sykes, Aftershock zones of great earthquakes, seismicity gaps, and  
622 earthquake prediction for Alaska and the Aleutians, *Journal of Geophysical*  
623 *Research* 76 (1971) 8021–8041. doi:10.1029/jb076i032p08021.

624 J. Davies, L. Sykes, L. House, K. Jacob, Shumagin Seismic Gap, Alaska  
625 Peninsula: History of great earthquakes, tectonic setting, and evidence for  
626 high seismic potential, *Journal of Geophysical Research* 86 (1981) 3821.  
627 doi:10.1029/JB086iB05p03821.

628 A. M. López, E. A. Okal, A seismological reassessment of the source of the  
629 1946 Aleutian 'tsunami' earthquake, *Geophysical Journal International*  
630 165 (2006) 835–849. doi:10.1111/j.1365-246X.2006.02899.x.

631 J. T. Freymueller, E. N. Suleimani, D. J. Nicolsky, Constraints on  
632 the Slip Distribution of the 1938  $M_w$  8.3 Alaska Peninsula Earth-  
633 quake From Tsunami Modeling, *Geophysical Research Letters* 48 (2021)  
634 e2021GL092812. doi:10.1029/2021GL092812.

635 C. H. Estabrook, K. H. Jacob, L. R. Sykes, Body wave and surface wave  
636 analysis of large and great earthquakes along the eastern Aleutian Arc,  
637 1923-1993: implications for future events, *Journal of Geophysical Research*  
638 99 (1994) 643–654. doi:10.1029/93jb03124.

639 Z. Lu, M. Wyss, G. Tytgat, S. McNutt, S. Stihler, Aftershocks of the 13  
640 May 1993 Shumagin Alaska earthquake, *Geophysical Research Letters* 21  
641 (1994) 497–500. doi:10.1029/94GL00332.

- 642 T. J. Fournier, J. T. Freymueller, Transition from locked to creeping sub-  
643 duction in the Shumagin region, Alaska, *Geophysical Research Letters* 34  
644 (2007) L06303. doi:10.1029/2006GL029073.
- 645 C. Drooff, J. T. Freymueller, New Constraints on Slip Deficit on the Aleutian  
646 Megathrust and Inflation at Mt. Veniaminof, Alaska From Repeat GPS  
647 Measurements, *Geophysical Research Letters* 48 (2021) e2020GL091787.  
648 doi:10.1029/2020GL091787.
- 649 C. H. Estabrook, T. M. Boyd, The Shumagin Islands, Alaska, earthquake of  
650 31 May 1917, *Bulletin of the Seismological Society of America* 82 (1992)  
651 755–773.
- 652 T. Lay, L. Ye, Y. Bai, K. F. Cheung, H. Kanamori, The 2018  $M_w$  7.9 Gulf of  
653 Alaska Earthquake: Multiple Fault Rupture in the Pacific Plate, *Geophys-  
654 ical Research Letters* 45 (2018) 9542–9551. doi:10.1029/2018GL079813.
- 655 S. Wei, D. Helmberger, J.-P. Avouac, Modeling the 2012 Wharton basin  
656 earthquakes off-Sumatra: Complete lithospheric failure, *Journal of Geo-  
657 physical Research: Solid Earth* 118 (2013) 3592–3609. doi:10.1002/jgrb.  
658 50267.
- 659 C. J. Ammon, H. Kanamori, T. Lay, A great earthquake doublet and seismic  
660 stress transfer cycle in the central Kuril islands, *Nature* 451 (2008) 561–  
661 565. doi:10.1038/nature06521.
- 662 Y. Tanioka, L. Ruff, K. Satake, The great Kurile Earthquake of October  
663 4, 1994 tore the slab, *Geophysical Research Letters* 22 (1995) 1661–1664.  
664 doi:10.1029/95GL01656.

- 665 R. A. Hansen, N. A. Ratchkovski, The Kodiak Island, Alaska  $M_w$  7 Earth-  
666 quake of 6 December 1999, *Seismological Research Letters* 72 (2001) 22–32.  
667 doi:10.1785/gssrl.72.1.22.
- 668 T. Lay, The surge of great earthquakes from 2004 to 2014, *Earth and*  
669 *Planetary Science Letters* 409 (2015) 133–146. doi:10.1016/j.epsl.2014.  
670 10.047.
- 671 J. Beavan, X. Wang, C. Holden, K. Wilson, W. Power, G. Prasetya, M. Bevis,  
672 R. Kautoke, Near-simultaneous great earthquakes at Tongan megathrust  
673 and outer rise in September 2009, *Nature* 466 (2010) 959–963. doi:10.  
674 1038/nature09292.
- 675 Y. Jiang, P. J. González, Bayesian Inversion of Wrapped Satellite Interfer-  
676 ometric Phase to Estimate Fault and Volcano Surface Ground Deforma-  
677 tion Models, *Journal of Geophysical Research: Solid Earth* 125 (2020).  
678 doi:10.1029/2019JB018313.
- 679 G. Blewitt, W. C. Hammond, C. Kreemer, Harnessing the gps data ex-  
680 plosion for interdisciplinary science, *Eos* 99 (2018) 1–2. doi:10.1029/  
681 2018E0104623.
- 682 E. H. Hearn, What can GPS data tell us about the dynamics of post-  
683 seismic deformation?, *Geophysical Journal International* 155 (2003) 753–  
684 777. doi:10.1111/j.1365-246X.2003.02030.x.
- 685 M. Bagnardi, A. Hooper, Inversion of Surface Deformation Data for Rapid  
686 Estimates of Source Parameters and Uncertainties: A Bayesian Approach,

687 Geochemistry, Geophysics, Geosystems 19 (2018) 2194–2211. doi:10.1029/  
688 2018GC007585.

689 C.-Y. Ke, G. C. McLaskey, D. S. Kammer, The Earthquake Arrest Zone,  
690 Geophysical Journal International (2020). doi:10.1093/gji/ggaa386.

691 G. P. Sendeckyj, Elastic inclusion problems in plane elastostatics, Interna-  
692 tional Journal of Solids and Structures 6 (1970) 1535–1543. doi:10.1016/  
693 0020-7683(70)90062-4.

694 R. M. J. Amey, A. Hooper, R. J. Walters, A Bayesian Method for Incorporat-  
695 ing Self-Similarity Into Earthquake Slip Inversions, Journal of Geophysical  
696 Research: Solid Earth 123 (2018) 6052–6071. doi:10.1029/2017JB015316.

697 B. W. Crowell, D. Melgar, Slipping the Shumagin Gap: A Kinematic Coseis-  
698 mic and Early Afterslip Model of the  $M_w$  7.8 Simeonof Island, Alaska,  
699 Earthquake, Geophysical Research Letters 47 (2020) e2020GL090308.  
700 doi:10.1029/2020GL090308.

701 L. Ye, T. Lay, H. Kanamori, Y. Yamazaki, K. F. Cheung, The 22 July 2020  
702  $M_w$  7.8 Shumagin seismic gap earthquake: Partial rupture of a weakly cou-  
703 pled megathrust, Earth and Planetary Science Letters 562 (2021) 116879.  
704 doi:10.1016/j.epsl.2021.116879.

705 R. Madariaga, Dynamics of an expanding circular fault, Bulletin of the  
706 Seismological Society of America 66 (1976) 639–666.

707 Y. Fukahata, T. J. Wright, A non-linear geodetic data inversion using ABIC  
708 for slip distribution on a fault with an unknown dip angle, Geophysi-



709 cal Journal International 173 (2008) 353–364. doi:10.1111/j.1365-246X.  
710 2007.03713.x.

711 G. C. P. King, R. S. Stein, J. Lin, Static stress changes and the triggering  
712 of earthquakes, Bulletin of the Seismological Society of America 84 (1994)  
713 935–953.

714 G. P. Hayes, G. L. Moore, D. E. Portner, M. Hearne, H. Flamme, M. Furtney,  
715 G. M. Smoczyk, Slab2, a comprehensive subduction zone geometry model,  
716 Science 362 (2018) 58–61. doi:10.1126/science.aat4723.

717 B. P. Allmann, P. M. Shearer, Global variations of stress drop for moderate  
718 to large earthquakes, Journal of Geophysical Research: Solid Earth 114  
719 (2009). doi:10.1029/2008JB005821.

720 T. Lay, Alaska EarthScope and Beyond, Feb 8: Thorne Lay and Carl Tape  
721 - MSU MediaSpace, 2021. URL: [https://mediaspace.msu.edu/media/  
722 Alaska+EarthScope+and+Beyond%2C+Feb+8A+Thorne+Lay+and+Carl+  
723 Tape/1\\_kmi3a07i](https://mediaspace.msu.edu/media/Alaska+EarthScope+and+Beyond%2C+Feb+8A+Thorne+Lay+and+Carl+Tape/1_kmi3a07i).

724 J. Li, D. J. Shillington, A. Bécel, M. R. Nedimović, S. C. Webb, D. M.  
725 Saffer, K. M. Keranen, H. Kuehn, Downdip variations in seismic reflection  
726 character: Implications for fault structure and seismogenic behavior in the  
727 Alaska subduction zone, Journal of Geophysical Research: Solid Earth 120  
728 (2015) 7883–7904. doi:10.1002/2015JB012338.

729 D. A. Oleskevich, R. D. Hyndman, K. Wang, The updip and downdip limits  
730 to great subduction earthquakes: Thermal and structural models of Casca-

- 731 dia, south Alaska, SW Japan, and Chile, *Journal of Geophysical Research:*  
732 *Solid Earth* 104 (1999) 14965–14991. doi:10.1029/1999jb900060.
- 733 M. Simoes, J. P. Avouac, R. Cattin, P. Henry, The Sumatra subduc-  
734 tion zone: A case for a locked fault zone extending into the man-  
735 tle, *Journal of Geophysical Research: Solid Earth* 109 (2004) 10402.  
736 doi:10.1029/2003JB002958.
- 737 J. R. Brown, S. G. Prejean, G. C. Beroza, J. S. Gomberg, P. J. Haeus-  
738 sler, Deep low-frequency earthquakes in tectonic tremor along the Alaska-  
739 Aleutian subduction zone, *Journal of Geophysical Research: Solid Earth*  
740 118 (2013) 1079–1090. doi:10.1029/2012JB009459.
- 741 X. Gao, K. Wang, Rheological separation of the megathrust seismogenic zone  
742 and episodic tremor and slip, *Nature* 543 (2017) 416–419. doi:10.1038/  
743 nature21389.
- 744 D. J. Shillington, A. Bécel, M. R. Nedimović, Active source seismic imaging  
745 in the area of the 2020 M7.8 Simeonof earthquake o the Alaska Peninsula,  
746 in: *2021 Alaska EarthScope and Beyond*, 2021, p. 01.
- 747 J. R. Weiss, Q. Qiu, S. Barbot, T. J. Wright, J. H. Foster, A. Saunders,  
748 B. A. Brooks, M. Bevis, E. Kendrick, T. L. Ericksen, J. Avery, R. S.  
749 Smalley, S. R. Cimbaro, L. E. Lenzano, J. Barón, J. C. Báez, A. Echalar,  
750 Illuminating subduction zone rheological properties in the wake of a giant  
751 earthquake, *Science Advances* 5 (2019) 6720–6738. doi:10.1126/sciadv.  
752 aax6720.

- 753 K. Wang, T. Huang, F. Tilmann, S. M. Peacock, D. Lange, Role of Ser-  
754 pentinized Mantle Wedge in Affecting Megathrust Seismogenic Behavior  
755 in the Area of the 2010 M8.8 Maule Earthquake, *Geophysical Research*  
756 *Letters* 47 (2020) e2020GL090482. doi:10.1029/2020GL090482.
- 757 A. H. Kohli, D. L. Goldsby, G. Hirth, T. Tullis, Flash weakening of serpen-  
758 tinite at near-seismic slip rates, *Journal of Geophysical Research* 116 (2011)  
759 B03202. doi:10.1029/2010JB007833.
- 760 J. R. Elliott, R. Jolivet, P. J. Gonzalez, J. P. Avouac, J. Hollingsworth,  
761 M. P. Searle, V. L. Stevens, Himalayan megathrust geometry and relation  
762 to topography revealed by the Gorkha earthquake, *Nature Geoscience* 9  
763 (2016) 174–180. doi:10.1038/ngeo2623.
- 764 J. Hubbard, R. Almeida, A. Foster, S. N. Sapkota, P. Bürgi, P. Tapponnier,  
765 Structural segmentation controlled the 2015  $M_w$  7.8 Gorkha earthquake  
766 rupture in Nepal, *Geology* 44 (2016) 639–642. doi:10.1130/G38077.1.
- 767 T. Seno, Subducted sediment thickness and  $M_w$  9 earthquakes, *Journal*  
768 *of Geophysical Research: Solid Earth* 122 (2017) 470–491. doi:10.1002/  
769 2016JB013048.
- 770 J. Li, D. J. Shillington, D. M. Saffer, A. Bécel, M. R. Nedimović, H. Kuehn,  
771 S. C. Webb, K. M. Keranen, G. A. Abers, Connections between subducted  
772 sediment, pore-fluid pressure, and earthquake behavior along the Alaska  
773 megathrust, *Geology* 46 (2018) 299–302. doi:10.1130/G39557.1.
- 774 S. Fuston, J. Wu, Raising the Resurrection plate from an unfolded-slab

- 775 plate tectonic reconstruction of northwestern North America since early  
776 Cenozoic time, *GSA Bulletin* (2020). doi:10.1130/b35677.1.
- 777 D. J. Shillington, A. Bécel, M. R. Nedimović, H. Kuehn, S. C. Webb, G. A.  
778 Abers, K. M. Keranen, J. Li, M. Delescluse, G. A. Mattei-Salicrup, Link  
779 between plate fabric, hydration and subduction zone seismicity in Alaska,  
780 *Nature Geoscience* 8 (2015) 961–964. doi:10.1038/ngeo2586.
- 781 Z. Li, D. Wiens, W. Shen, Crust and Uppermost Mantle Structure of the  
782 Alaska Subduction Zone from Joint Inversion of Rayleigh Wave Dispersion  
783 and Receiver Functions, in: AGU fall meeting, 2020, pp. T055–04.
- 784 D. Turcotte, G. Schubert, Elasticity and Flexure, in: *Geodynam-*  
785 *ics*, Cambridge University Press, 2014, pp. 130–159. doi:10.1017/  
786 CB09780511843877.004.
- 787 F. Zhang, J. Lin, Z. Zhou, H. Yang, W. Zhan, Intra- and intertrench varia-  
788 tions in flexural bending of the Manila, Mariana and global trenches: im-  
789 plications on plate weakening in controlling trench dynamics, *Geophysical*  
790 *Journal International* 212 (2018) 1429–1449. doi:10.1093/gji/ggx488.
- 791 M. W. Herman, K. P. Furlong, Triggering an unexpected earthquake in an  
792 uncoupled subduction zone, *Science Advances* 7 (2021) eabf7590. doi:10.  
793 1126/sciadv.abf7590.